Polar Coordinate Fourier single-pixel imaging

Article *in* Optics Letters · January 2023

DOI: 10.1364/OL.479806

Guan Wang
Hefei University of Technology

H. Deng
Hefei University of Technology

Mengchao Ma
Hefei University of Technology

Optics Letters

Polar coordinate Fourier single-pixel imaging

GUAN WANG,[1] HUAXIA DENG,[2,*] MENGCHAO MA,[1] AND XIANG ZHONG[1]

[1]School of Instrument Science and Opto-Electronics Engineering, Hefei University of Technology, Hefei, Anhui 230009, China
[2]CAS Key Laboratory of Mechanical Behavior and Design of Materials, Department of Modern Mechanics, University of Science and Technology of China, Hefei 230027, China
*Corresponding author: hxdeng@ustc.edu.cn

Received 2 November 2022; revised 27 December 2022; accepted 3 January 2023; posted 3 January 2023; published 26 January 2023

Traditional single-pixel imaging uses Fourier patterns to modulate objects in the Cartesian coordinate system. The Cartesian Fourier pattern of single-pixel imaging is inappropriate to display in a circular field of view. However, a circular field of view is a widespread form of display in computed optical imaging. Here, circular patterns are adopted to adapt to the circular visual area. The circular patterns are displayed in polar coordinates and derived from two-dimensional Fourier transform in polar coordinates. The proposed circular patterns have improved imaging efficiency significantly from 63.66% to 100%. The proposed polar coordinate Fourier single-pixel imaging is expected to be applied in circular field-of-view imaging and foveated imaging.

https://doi.org/10.1364/OL.479806

Foveated imaging mimics the human visual system [1,2], which grasps active foveation of the area of interest with high angular resolution across a circular visual field. With these unique characteristics, foveated imaging provides a much higher resolution in terms of capturing target detail compared to uniform resolution imaging acquisition under the same pixel condition. Increasing pixel number is a severe obstacle for single-pixel imaging, which reconstructs an image through massive patterns. Thus, foveated imaging is a natural algorithm for single-pixel imaging to improve target detail recognition in the circular visual field. However, the patterns employed in single-pixel imaging are generated under Cartesian coordinates, which cannot make the most use of the circular field of view [3–7].

There are four main ways to realize foveated imaging: multi-camera systems; optical lens design; foveated imaging sensors; and computational methods. The multi-camera system consists of different focal length cameras so that images with various fields of view are obtained by different cameras. Then, these images are integrated to achieve both a large field of view and foveated imaging [8]. To reduce the number of cameras, optical lens designing is proposed to achieve foveated imaging with only one camera. The optical lens design of the camera is derived from the distortion characteristic of the lens [9]. With the development of array detectors, foveated CCD sensors exhibit high resolution in the center of sensors and a relatively poor resolution on the edge. Foveated CCD sensors are manufactured to achieve foveated imaging, mimic the human visual system, and be capable of adapting to various conditions [10]. Recent research in computational methods such as computer vision is also used to achieve foveated imaging [11,12]. Compared to traditional foveated imaging methods, the computational method transfers the difficulty from the manufacturing technique to algorithm optimization.

Single-pixel imaging [7,13–15], a method of computational imaging, uses a photodetector (PD) instead of array detector and encodes spatial information in the temporal dimension. To obtain spatial information, multiple patterns have to be generated to modulate a single object. For example, 250,000 random square patterns are needed for reconstructing the object with 500×500 resolution [16,17]. To achieve the same 500×500 level of resolution with fewer patterns, single-pixel imaging using Hadamard or Fourier square patterns is proposed. The Hadamard or Fourier technique is able to reduce the number of patterns used by one order of magnitude—25,000 [4,18,19]. The number of patterns needed increases explosively for higher resolution, such as 1024×1024. Regardless of random, Hadamard, and Fourier patterns, increasing pixel numbers is a tremendous obstacle for single-pixel imaging. Therefore, to achieve higher resolution and, at the same time, limit the number of patterns used, a new method of single-pixel imaging is pressing.

Foveated imaging provides a new approach for single-pixel imaging to improve the image resolution [20,21]. A satisfactory resolution is obtained in the region of interest (ROI) by illuminating the object without requiring the explosive spike of patterns needed. Traditional Fourier single-pixel imaging are encoded in Cartesian coordinates, and square patterns are often employed. However, a microscope and optical fiber mostly entail circular visual fields. Therefore, research for circular patterns is necessary.

In this paper, the circular polar coordinate Fourier pattern (CPCFP) is proposed to be employed in single-pixel imaging. CPCFP is compatible with a circular visual field. We have demonstrated that single-pixel imaging using circular patterns is more efficient in a circular visual field compared to using square patterns. The reconstructed image quality is better when demonstrated using CPCFP in comparison to the traditional method. The paper is organized as follows. First, the principle of CPCFP is demonstrated. Then, simulation and experiment of single-pixel imaging are conducted using CPCFP, and the quality of the reconstructed image is analyzed. Finally, microscopy experiments with different compressed sampling ratios are demonstrated.

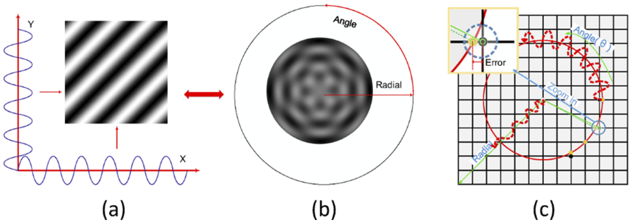

Fig. 1. (a) Square pattern in the Cartesian coordinate system. (b) Circular pattern transformed from a Cartesian coordinate system to a polar coordinate system. (c) Numerical approximation error of the circular pattern in the left transformation.

In the traditional foveated single-pixel imaging, randomly distributed mosaic patterns are employed accordingly for optical modulation [21]. However, circular Fourier pattern modulation is derived from polar Fourier transform (PFT), in which all signals including 1D and 2D signals can be decomposed into the combination of cosine curves and Bessel curves of different frequencies. Low-frequency signals have higher weight coefficients compared to high-frequency signals. Accordingly, a small amount of low-frequency data is adequate for reconstructing the original signals. To conduct compressed single-pixel imaging under a circular field of view, we generated CPCFP with different frequencies. Here, the Fourier patterns are transformed from square to circular to fit the circular field of view. In the polar coordinate system, each point or line is determined by two independent variables—angle coordinate (θ) and radial coordinate (r), corresponding to abscissa (x) and ordinate (y) in the Cartesian coordinate system. As is shown in Fig. 1, the two-dimensional sinusoidal pattern in the Cartesian coordinate system is transformed into a circular sinusoidal pattern in the polar coordinate system. The variables of r and θ in the polar coordinate system are expressed mathematically as

$$r=\sqrt{(x-x_0)^2+(y-y_0)^2}, \tag{1}$$

$$\theta=\begin{cases}\arccos\left(\frac{x-x_0}{r}\right), & y\leq y_0,\\ 2\pi-\arccos\left(\frac{x-x_0}{r}\right), & y>y,\end{cases} \tag{2}$$

where (x_0, y_0) represents the center of the circular patterns.

Figure 2 shows the efficiency of square patterns used in a circular field of view. Obviously, four corners of the object are unavailable due to square patterns modulation in the circular field of view. Therefore, the efficiency of square patterns η is

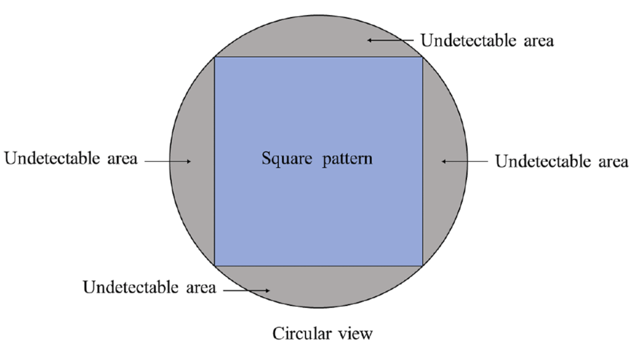

Fig. 2. Demonstration of the square pattern in the circular visual field. The square pattern is unadapted to the circular visual field. The four corners of the object are undetectable areas in the circular field of view.

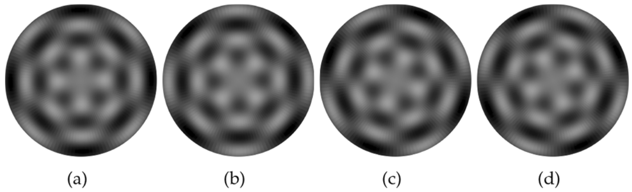

Fig. 3. Sequence of proposed two-dimensional circular patterns. (a)–(d) Set of patterns with a four-step phase shift $0, \frac{\pi}{2}, \pi, \frac{3\pi}{2}$. More details are given in Supplement 1.

calculated as

$$\eta=\frac{S_s}{S_c}=\frac{d^2}{\pi r^2}=\frac{2}{\pi}=63.66\%, \tag{3}$$

where S_c and S_s are areas of the circular pattern and square pattern, respectively, and r and d are the radius and diameter of the circular field of view, respectively. The efficiency of the circular pattern is 100% while the efficiency of the square pattern is only 63.66%. We can see that the square pattern could be amplified to cover the circular field of view, but the four corners are useless and redundant for circular single-pixel imaging.

To improve the imaging efficiency, a sequence of circular Fourier patterns is proposed in Fig. 3. The circular Fourier pattern P is mathematically expressed as

$$\mathrm{P}(r,\theta;\phi)=2\frac{J_n\left(\frac{j_{nk}j_{nl}}{j_{nN_1}}\right)}{j_{nN_1}J^2_{n+1}(j_{nk})}\cos(\frac{2\pi np}{N_2}+\phi), \tag{4}$$

where $\phi=0, \frac{\pi}{2}, \pi, \frac{3\pi}{2}$. Here, $r=\frac{j_{pk}R}{j_{pN_1}}$ and $\theta=\frac{2\pi p}{N_2}$, where r and θ are the radial and angular coordinates in the spatial domain, respectively. Additionally, R is the space limit, n is the order of the Bessel function, J_n. Furthermore, j_{nk}, j_{nl}, and j_{nN_1} are the kth, lth, and N_1th zeros of the n-order Bessel curve, respectively (see Supplement 1 for a full description). Here, the diameter of the patterns is 127. The center of the patterns is located at the Cartesian coordinate (64,64). The radial unit is 1, and the angle unit is $\frac{2\pi}{127}$. There are $127\times127\times4=64,516$ different circular patterns in total, for a four-step phase shift.

The frequency components of the reconstructed object, expressed in the proposed polar coordinate, are measured by

$$F(n,l)=\sum_{k=0}^{N_1-2}\sum_{p=-M}^{M}\mathrm{P}(r,\theta)\,\mathrm{f}(k,p). \tag{5}$$

In Eq. (5), $p=-M\sim M$, $l=0\sim N_1-2$. Here, N_1 is the number of sample points in the radial direction, $\mathrm{f}(k,p)$ refers to the object to be reconstructed, $F(n,l)$ is the frequency information in polar coordinate and is obtained through measuring the photoelectric response in the process of the pattern modulation.

$$F(q,l)=\sum_{n=-M}^{M}F(n,l)e^{\frac{2\pi inq}{N2}}. \tag{6}$$

The frequency components of the object expressed in polar coordinates are then obtained by the Fourier transform of $F(n,l)$. In Eq. (6), the variable n of the Bessel function order is transformed to angle frequency component q in the polar coordinate.

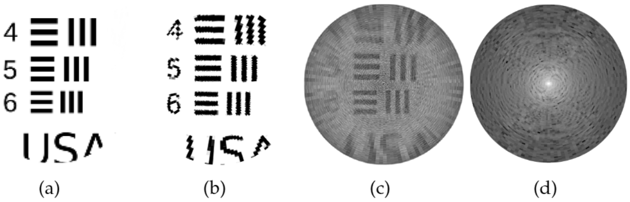

Fig. 4. Simulation and experimental result. (a) USAF-1951 target object to be reconstructed. (b) Simulation result of the target. (c) Experimental result of the target. (d) Energy distribution in the polar Fourier spectrums of the target.

After all frequency components of the object are measured, the object could be reconstructed by

$$\mathrm{f}(k, p) = \mathrm{IPFT}(F(q, l)), \tag{7}$$

where IPFT refers to inverse polar coordinate Fourier transform. Object f, the target to be recovered, is reconstructed through IPFT.

Here, the simulation experiment that reconstructs image of the target using the proposed CPCFP is validated. The object to be recovered is USAF-1951 target in Fig. 4(a). The result is shown in Fig. 4(b). An experiment of CPCFP single-pixel imaging is achieved in the following scene. Sequences of CPCFP are projected onto the object by a digital light projector. The reflected lights are measured by a PD, which is used to calculate Fourier data in the frequency domain. In the experiment, the diameter of the proposed circular patterns is 127. We successfully measured 100% of the frequency data for USAF-1951 target reconstruction. The number of CPCFPs used to modulate the target is 64,516. The reconstructed target is shown in Fig. 4(c). The Fourier spectrums are shown in Fig. 4(d).

We have demonstrated that compressed sampling is also efficient in the proposed CPCFP of polar coordinate single-pixel imaging, except for Cartesian coordinate Fourier single-pixel imaging. The sequence of the CPCFP is symmetrical along angle frequencies, as shown in Eq. (8), so half of the measurements are redundant:

$$J_{-\alpha}(x) = (-1)^{\alpha} J_{\alpha}(x). \tag{8}$$

Here, α is 1 to 63 for the angle size of 127. It means that the target can be reconstructed using undersampling technology. We used simple square sampling as our frequency sampling strategy for demonstration. As shown in Fig. 5, the frequencies along the angle and radial directions are rearranged to the

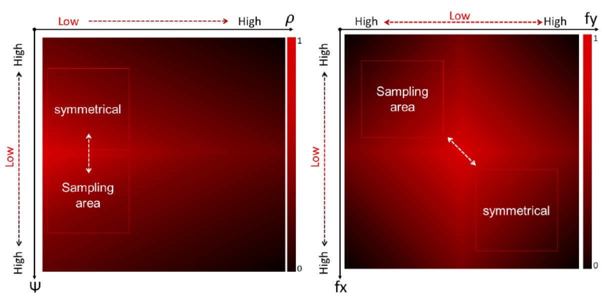

(a) (b)

Fig. 5. (a) Frequency sampling strategy in the polar coordinate Fourier single-pixel imaging. (b) Frequency sampling strategy in the Cartesian coordinate Fourier single-pixel imaging.

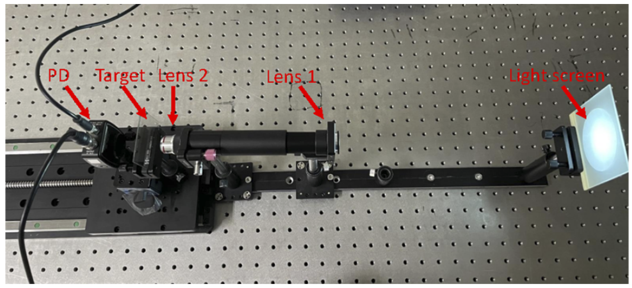

Fig. 6. Polar coordinate Fourier single-pixel microscopy imaging.

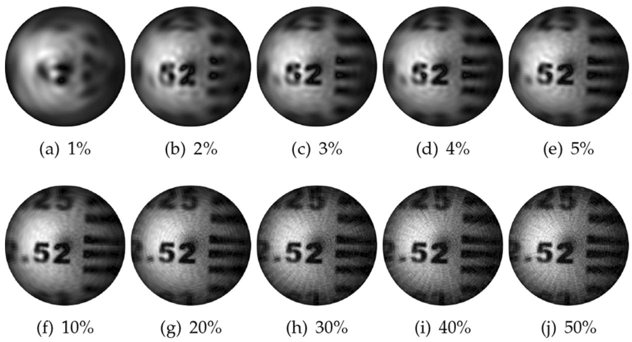

Fig. 7. Polar coordinate Fourier single-pixel microscopy imaging results using the undersampling method: (a) 1% frequency; (b) 2% frequency; (c) 3% frequency; (d) 4% frequency; (e) 5% frequency; (f) 10% frequency; (g) 20% frequency; (h) 30% frequency; (i) 40% frequency; (j) 50% frequency.

array. We sampled the area from low frequency to high frequency [Fig. 5(a)], similar to the sampling strategy adopted in the Cartesian coordinate Fourier single-pixel imaging [Fig. 5(b)].

To demonstrate the advantage of the proposed CPCFP modulation method, we have setup a microscopy light path to perform circular Fourier single-pixel imaging. As shown in Fig. 6, an optical screen is used for displaying modulation patterns, and the patterns are then imaged on the target by microscopic lenses 1 and 2. The modulated light is measured by a PD finally. The patterns that modulate the target are circular, adapted to the circular field of view in the lens imaging path. The size of the pattern is 127×127 along the angle and radial directions, respectively. As shown in Fig. 7, we have demonstrated microscopy imaging under sampling ratios of 1%, 2%, 3%, 4%, 5%, 10%, 20%, 30%, 40%, and 50%. The center area of the microscopy field of view is reconstructed with higher resolution compared to the surroundings. Particularly, the reconstruction quality of the center area is satisfactory when the sampling ratio is above 2%.

The performance of the proposed CPCFP single-pixel imaging is satisfactory in the center area with fewer patterns modulation. We have demonstrated modulation performance in comparison with the traditional Fourier single-pixel imaging. The reconstructed target in the Cartesian coordinate showcased the difference. As shown in Figs. 8(a)–8(c), the target is recovered using patterns under Cartesian coordinates. The size of the used patterns is 128×128 along the x and y axes, respectively. Figures 8(d)–8(f) are the recovered target using polar coordinate patterns modulation, and the size of patterns is 127×63 along angle and radial, respectively. Figure 8(g)–(i) are still the recovered target using polar coordinate patterns modulation, but

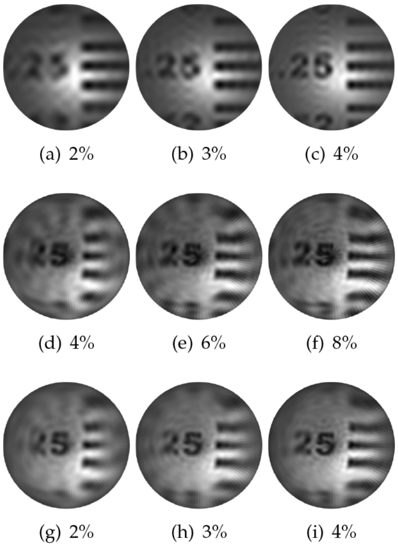

Fig. 8. (a)–(c) Size of 128×128. Results are recovered by Cartesian coordinate Fourier single-pixel imaging and the sampling ratios are 2%, 3%, and 4% respectively. (d)–(f) Size of 127×63. Results are recovered by polar coordinate Fourier single-pixel imaging and the sampling ratios are 4%, 6%, and 8%, respectively. (g)–(i) Size of 127×127. Results are recovered by polar coordinate Fourier single-pixel imaging, and the sampling ratios are 2%, 3%, and 4%, respectively.

the size of patterns is 127×127 along angle and radial directions, respectively. The results in each column of Fig. 8 are reconstructed with the same number of modulation patterns. Comparing results in rows one and two, we can see that the foveated area recovered by the CPCFP modulation method is better under the same compressed sampling rate. The quality of the foveated area converges rapidly using polar coordinate patterns. During the process of foveated imaging, the center area is reconstructed well at the cost of its surrounding area being blurred. By comparing results in row two and row three, it is also clear that the resolution of reconstructed center area is enhanced by increasing the pattern size from 63 to 127 along the radial direction.

We have demonstrated single-pixel imaging based on polar coordinate FT to adapt to a circular field of view. The proposed imaging method's modulation patterns are naturally circular and foveated. Compared to traditional single-pixel imaging based on the Cartesian coordinate Fourier transform, the proposed method has the advantage of foveated imaging, which is expected to be applied in a large field of view imaging.

In conclusion, the proposed CPCFP single-pixel imaging is applied appropriately in the circular field of view. Compared to the efficiency of a square Fourier pattern in Cartesian coordinates, the efficiency of the CPCFP increased from 63.66% to 100%. In addition, the proposed polar coordinate Fourier single-pixel imaging is naturally suitable for foveated imaging since pixels of the reconstructed image are convergent in the center area and divergent in the outer area.

Funding. Natural Science Foundation of Anhui Province (1908085J15, 2208085ME138); National Natural Science Foundation of China (11872167, 52275529).

Disclosures. The authors declare that they have no competing interests.

Data availability. Data underlying the results presented in this paper are not publicly available at this time but may be obtained from the authors upon reasonable request.

Supplemental document. See Supplement 1 for supporting content.

REFERENCES

1. Y. Qin, H. Hua, and M. Nguyen, Opt. Lett. **38**, 2191 (2013).
2. G. Carles, S. Chen, N. Bustin, J. Downing, D. McCall, A. Wood, and A. R. Harvey, Opt. Lett. **41**, 1869 (2016).
3. L. Bian, J. Suo, Q. Dai, and F. Chen, J. Opt. Soc. Am. A **35**, 78 (2018).
4. Z. Zhang, S. Liu, J. Peng, M. Yao, G. Zheng, and J. Zhong, Optica **5**, 315 (2018).
5. L. Bian, J. Suo, G. Situ, Z. Li, J. Fan, F. Chen, and Q. Dai, Sci. Rep. **6**, 24752 (2016).
6. R. Dutta, S. Manzanera, A. Gambín-Regadera, E. Irles, E. Tajahuerce, J. Lancis, and P. Artal, Biomed. Opt. Express **10**, 4159 (2019).
7. M. P. Edgar, G. M. Gibson, and M. J. Padgett, Nat. Photonics **13**, 13 (2019).
8. S. Thiele, K. Arzenbacher, T. Gissibl, H. Giessen, and A. M. Herkommer, Sci. Adv. **3**, 1602655 (2017).
9. N. Hagen and T. S. Tkaczyk, J. Biomed. Opt. **17**, 021104 (2012).
10. E. Akbas and M. P. Eckstein, PLoS Comput. Biol. **13**, e1005743 (2017).
11. R. Frame, IEEE Trans. Visual. Comput. Graphics **26**, 1972 (2020).
12. A. S. Kaplanyan, A. Sochenov, T. Leimkühler, M. Okunev, T. Goodall, and G. Rufo, ACM Trans. Graph. **38**, 212 (2019).
13. N. Radwell, K. J. Mitchell, G. M. Gibson, M. P. Edgar, R. Bowman, and M. J. Padgett, Optica **1**, 285 (2014).
14. G. S. D. Gordon, J. Joseph, S. E. Bohndiek, and T. D. Wilkinson, J. Lightwave Technol. **33**, 3419 (2015).
15. M. Sun and J. Zhang, Sensors **19**, 732 (2019).
16. B. Sun, S. S. Welsh, M. P. Edgar, J. H. Shapiro, and M. J. Padgett, Opt. Express **20**, 16892 (2012).
17. S. Jiang, X. Li, Z. Zhang, W. Jiang, Y. Wang, G. He, Y. Wang, and B. Sun, Opt. Express **27**, 22499 (2019).
18. M. F. Duarte, M. A. Davenport, D. Takhar, J. N. Laska, T. Sun, K. F. Kelly, and R. G. Baraniuk, IEEE Signal Process. Mag. **25**, 83 (2008).
19. Z. Zhang, X. Ma, and J. Zhong, Nat. Commun. **6**, 6225 (2015).
20. D. Phillips, M. Sun, J. M. Taylor, M. Edgar, S. M. Barnett, G. M. Gibson, and M. J. Padgett, Sci. Adv. **3**, 1601782 (2017).
21. X. Zhai, Z. Cheng, Y. Hu, Y. Chen, Z. Liang, and Y. Wei, Opt. Commun. **448**, 69 (2019).